Biomaterials xxx (2018) 1–13

Contents lists available at ScienceDirect

Biomaterials

journal homepage: www.elsevier.com/locate/biomaterials

3D printing of a lithium-calcium-silicate crystal bioscaffold with dual bioactivities for osteochondral interface reconstruction

Lei Chen [a, 1], Cuijun Deng [a, b, 1], Jiayi Li [c], Qingqiang Yao [c, **], Jiang Chang [a, ***], Liming Wang [c], Chengtie Wu [a, *]

[a] State Key Laboratory of High Performance Ceramics and Superfine Microstructure, Shanghai Institute of Ceramics, Chinese Academy of Sciences, Shanghai, 200050, PR China
[b] University of Chinese Academy of Sciences, Beijing, 100049, PR China
[c] Department of Orthopaedic Surgery, Digital Medicine Institute, Nanjing Medical University Nanjing Hospital, No. 68 Changle Road, Nanjing, 210006, PR China

ARTICLE INFO

Article history:
Received 13 December 2017
Received in revised form
21 March 2018
Accepted 2 April 2018
Available online xxx

Keywords:
Scaffolds
Lithium calcium silicate
Dual bioactivity
Osteochondral reconstruction
Tissue engineering

ABSTRACT

It is difficult to achieve self-healing outcoming for the osteochondral defects caused by degenerative diseases. The simultaneous regeneration of both cartilage and subchondral bone tissues is an effective therapeutic strategy for osteochondral defects. However, it is challenging to design a single type of bioscaffold with suitable ionic components and beneficial osteo/chondral-stimulation ability for regeneration of osteochondral defects. In this study, we successfully synthesized a pure-phase lithium calcium silicate ($Li_2Ca_4Si_4O_{13}$, $L_2C_4S_4$) bioceramic by a sol-gel method, and further prepared $L_2C_4S_4$ scaffolds by using a 3D-printing method. The compressive strength of $L_2C_4S_4$ scaffolds could be well controlled in the range of 15–40 MPa when pore size varied from 170 to 400 μm. $L_2C_4S_4$ scaffolds have been demonstrated to possess controlled biodegradability and good apatite-mineralization ability. At a certain concentration range, the ionic products from $L_2C_4S_4$ significantly stimulated the proliferation and maturation of chondrocytes, as well as promoted the osteogenic differentiation of rBMSCs. $L_2C_4S_4$ scaffolds simultaneously promoted the regeneration of both cartilage and subchondral bone as compared to pure β-TCP scaffolds in rabbit osteochondral defects. These findings suggest that 3D-printed $L_2C_4S_4$ scaffolds with such specific ionic combination, high mechanical strength and good degradability as well as dual bioactivities, represent a promising biomaterial for osteochondral interface reconstruction.

1. Introduction

Articular cartilage lesion is one of the most challenging issues in orthopedic and sports medicine due to the poor self-healing capability of cartilage. Numerous approaches, such as abrasion arthroplasty, chondral drilling, microfracturing, mosaicplasty and autologous chondrocyte implantation, have been used for treating the patients suffered from chondral pain [1]. However, the treatments are limited by their own disadvantages [2]. Increasing evidences show that articular cartilage defects always extend deeply into subchondral bone tissue [3]. Intensive interaction between articular cartilage and subchondral bone is essential for the maintenance of cartilage-bone interface [4,5]. Hence, simultaneous regeneration of both cartilage and subchondral bone tissues is of great importance to develop the targeted and effective therapeutic strategies for treating osteochondral defects [6].

Among these strategies, three-dimensional (3D) porous scaffolds with proper biodegradability are often used as a matrix material to support cell adhesion, guide tissue formation and restore organ function [7–9]. Since cartilage and subchondral bone tissues have different components and distinct lineage-specific biological properties, indicating the complexity of two tissue interface between bone and cartilage. Thus, it is difficult to design and fabricate a bi-lineage scaffold for osteochondral defect regeneration. Previously, various types of scaffolds, including monophasic, biphasic and triphasic scaffolds, have been developed for regeneration of osteochondral defects [10–12], whereas the insufficient bonding

* Corresponding author.
** Corresponding author.
*** Corresponding author.
E-mail addresses: yaoqingqiang@126.com (Q. Yao), jchang@mail.sic.ac.cn (J. Chang), chengtiewu@mail.sic.ac.cn (C. Wu).
[1] L. C and C.D are co-first authors.

https://doi.org/10.1016/j.biomaterials.2018.04.005
0142-9612/

force between two layers of multilayered scaffolds restricts their application. Although multilayered scaffolds have been developed for mimicking the microstructure of cartilage and subchondral tissues, it is difficult to imitate the physiological structure and functions of cartilage and subchondral bone due to the complex interface [13–16]. A number of natural and synthetic biomaterials, such as collagen, poly (caprolactone), calcium phosphates and silicate bioactive glasses, have been used to generate scaffolds for cartilage or bone defect regeneration [17–22]. Nevertheless, few of these materials could simultaneously regenerate both of cartilage and subchondral bone. Hence, the biomaterial with dual bioactivities for simultaneously regenerating both cartilage and subchondral bone is highly demanded.

For reconstruction of osteochondral defects, it is needed to synthesize new bioactive materials which possess bioactive components. Silicon (Si) is one of the bioactive constituents in human body, which localizes in the active calcification sites of young bone and involves in the early mineralization process during new bone formation [23,24]. Based on the advantages, Si has been widely incorporated into biomaterials to improve biological performance [25–27]. Previously, silicate bioceramics have been found to significantly stimulate the proliferation and bone-related genes expression of several stem cells, indicating that silicate bioceramics have the potential to enhance osteogenesis and promote bone regeneration [22,28–32]. Furthermore, Si plays a key role in cartilage system and has a positive impact on the synthesis of cartilage extracellular matrix [33,34]. Lithium (Li), a drug for the treatment of depressive disorder [35] was proved to have significantly therapeutic potential for arthritis therapy. It was found that the chemical LiCl salt could stimulate subchondral bone formation and enhance bone mass in mice via activation of the Wnt signaling pathway [36]. LiCl had been reported to selectively inhibit the phosphorylation and protect cartilage from degradation [37–39]. Recent studies suggested that Li could stimulate chondrocyte proliferation and modulate the primary cilia of chondrocytes [40,41]. Therefore, we supposed that if we can synthesize a new compound with incorporation of Si and Li as well as other elements, which may be used for regeneration of osteochondral defects by using the unique bioactivities of two ions. Lithium calcium silicate ($Li_2Ca_4Si_4O_{13}$, $L_2C_4S_4$) is a Li-containing silicate material. Previously, $L_2C_4S_4$ powders were synthesized by a solid-state method, but the synthetic steps were quite complicated and time-consuming [42]. In this study, high purity of $L_2C_4S_4$ powders were firstly synthesized via a sol-gel method and $L_2C_4S_4$ scaffolds were fabricated by using 3D-printing. Taking advantages of the cooperative effect of Li and Si ions, it was supposed that $L_2C_4S_4$ scaffolds could regenerate both of cartilage and subchondral bone simultaneously. The physicochemical properties, *in vitro* and *in vivo* bioactivity of $L_2C_4S_4$ scaffolds for osteochondral regeneration were systematically investigated. (see Scheme 1)

2. Materials and methods

2.1. Synthesis and characterization of $L_2C_4S_4$ powders

$L_2C_4S_4$ powders were synthesized by a sol-gel process using tetraethyl orthosilicate ($(C_2H_5O)_4Si$, TEOS), calcium nitrate tetrahydrate ($Ca(NO_3)_2{\cdot}4H_2O$) and lithium nitrate ($LiNO_3$) as raw materials (all from Sinopharm Chemical Reagent Co., Ltd, Shanghai, China). Briefly, the TEOS was mixed with distilled water and 2M HNO_3 (mol ratio: TEOS/distilled water/HNO_3 = 1: 8: 0.16) then hydrolyzed for 30 min under stirring. Subsequently, $LiNO_3$ and $Ca(NO_3)_2{\cdot}4H_2O$ were added into the mixture (mol ratio: TEOS/$Ca(NO_3)_2{\cdot}4H_2O$/$LiNO_3$ = 2:2:1), and these reactants were stirred for 5 h at room temperature to get transparent solution. After the reaction, the solution was maintained at 60 °C for 24 h to form transparent gels and then dried at 120 °C for 2 days to obtain xerogels. The xerogels were ground, sieved to 200-mesh and calcined at different temperatures (500 °C, 600 °C, 800 °C and 940 °C) for 3 h with a heating rate of 2 °C/min. The dry gel was tested by thermal analysis - mass spectrometer (Netzsch STA 449C, Germany). The calcined powders were characterized by X-ray diffractometer (XRD, Geigerflex, Rigaku Co., Japan) using Cu Kα radiation and operating at 40 KV with 40 mA current. The 2θ angles were scanned from 10° to 80° at a scanning rate of 5°/min. The morphology of $L_2C_4S_4$ powders was observed by a HITACHI SU8220 scanning electron microscope (SEM, Hitachi, Japan).

2.2. 3D-printing preparation of $L_2C_4S_4$ scaffolds

The 3D-printing device (3D scaffold printer) applied in this study was developed by the Fraunhofer Institute for Materials Research and Beam Technology (Dresden, Germany). The principle of this device was based on a precision three-axis positioning system (Nano- Plotter NP 2.1, GeSiM, Grosserkmannsdorf, Germany). Sodium alginate (Alfa Aesar, low viscosity) and Pluronics F-127 (Sigma-Aldrich, USA) were selected as binder, which were water-soluble and could be easily burned off while sintering the scaffolds. Injectable $L_2C_4S_4$ inks were prepared by mixing 1.8 g of $L_2C_4S_4$ powders with 0.1 g sodium alginate powders, and then adding 1.8 g of Pluronics F-127 solution (20 wt%). After homogeneously stirring, the inks were loaded into printing tubes, and $L_2C_4S_4$ scaffolds were generated through 3D printing via a dosing pressure of 1.5–2.5 bar and a moving speed of 3 mm/s. The printed scaffolds were dried at room temperature for 24 h and then sintered at 960 °C for 3 h to obtain $L_2C_4S_4$ scaffolds. As the control materials, β-TCP scaffolds were prepared by the same method and sintered at 1100 °C for 3 h.

2.3. Characterization of $L_2C_4S_4$ scaffolds

The phase compositions of $L_2C_4S_4$ scaffolds were analyzed by XRD. The morphology, pore structure and pore size of the $L_2C_4S_4$ scaffolds were observed by optical microscopy (S6D, Leica, Germany) and SEM, and elemental analysis was carried out by using an energy dispersive spectrometer (EDS,SU8220, Hitachi, Japan).

Simulated body fluids (SBF), which were prepared according to previous method [43], were selected to investigate the apatite mineralization ability of $L_2C_4S_4$ scaffolds *in vitro*. $L_2C_4S_4$ scaffolds were soaked in SBF at 37 °C for 14 days, and the ratio of the solution volume to the scaffold mass was 200 mL g^{-1}. The SBF solution was refreshed after soaking for 1, 3, 7 and 10 days, respectively. The scaffolds were collected from SBF solution after soaking 14 days, rinsed with distilled water for 3 times and dried at 60 °C overnight. The apatite formation on the surfaces of scaffolds was observed by XRD, SEM and EDS.

2.4. Mechanical property of $L_2C_4S_4$ scaffolds

To control the scaffold pore size and porosity, different printing parameters can be selected. In this study, three kinds of macropore sizes (170, 250, 400 μm) were designed and printed for mechanical testing. The compressive strength of $L_2C_4S_4$ scaffolds (Ø5.5 × 6.8 mm) was measured using a computer controlled universal testing machine (AG-I, Shimadzu, Japan) at a cross-head speed of 0.5 mm min^{-1}. Six scaffolds per group were tested to obtain an average value of the mechanical strength. The pore structure and porosity of $L_2C_4S_4$ scaffolds were obtained by using a micro-computed tomography (Micro-CT) system (Skyscan 1172, Bruker, Belgium).

Please cite this article in press as: L. Chen, et al., 3D printing of a lithium-calcium-silicate crystal bioscaffold with dual bioactivities for osteochondral interface reconstruction, Biomaterials (2018), https://doi.org/10.1016/j.biomaterials.2018.04.005

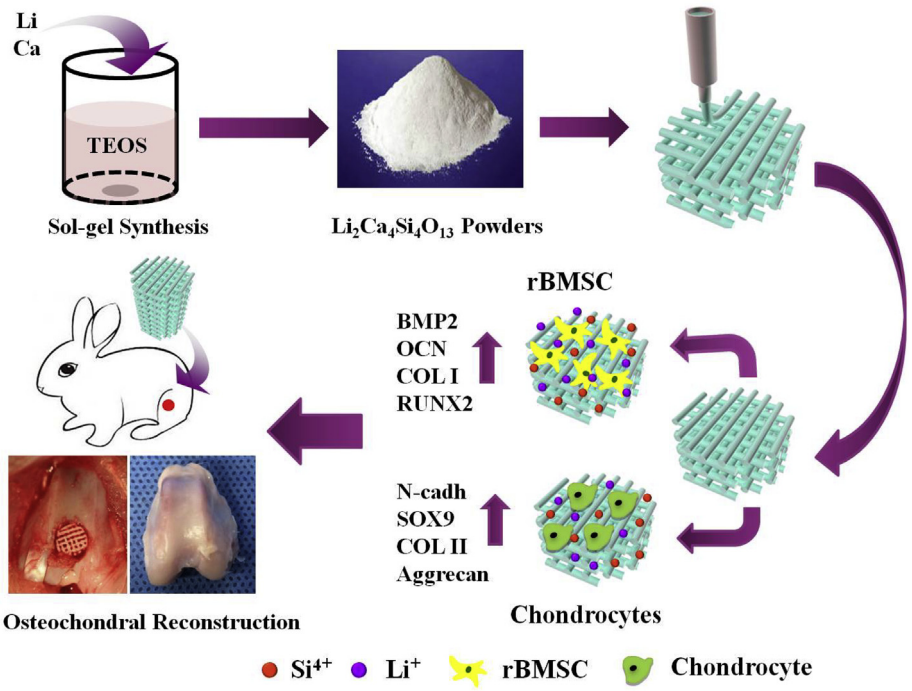

Scheme 1. Schematic illustration of application of $Li_2Ca_4Si_4O_{13}$ scaffolds for osteochondral reconstruction. The pure-phase $Li_2Ca_4Si_4O_{13}$ powders were successfully synthesized by a sol-gel method. 3D-printed $Li_2Ca_4Si_4O_{13}$ scaffolds not only promoted cartilage maturation, but also stimulated osteogenic differentiation *in vitro*; on the other hand, $Li_2Ca_4Si_4O_{13}$ scaffolds significantly accelerated cartilage regeneration as well as promoted subchondral bone reconstruction *in vivo*.

2.5. Degradation property of $L_2C_4S_4$ scaffolds

Tris-HCl was selected to evaluate the degradation of $L_2C_4S_4$ scaffolds as it did not contain inorganic ions (e.g., Ca, P and Si). $L_2C_4S_4$ scaffolds were soaked in Tris-HCl solution (pH 7.40) at 37 °C for different time periods. The ratio of the solution volume to the scaffold mass was 200 mL g^{-1}. After 1, 3, 7, 10, 14, 21 and 35 days of soaking, the pH values of the solution were measured by using an electrolyte type pH meter (PHS-2C, Jingke Leici Co., Shanghai, China) without refreshment of the immersion medium. After the set soaking time, the scaffolds were dried at 120 °C for 1 day and the final weight of each sample was accurately measured. The weight loss was expressed as percentage of the initial weight. To assess ionic release from scaffolds, the immersion solutions were updated and collected at every time period. The concentrations of Ca, Si, P and Li ions in the collected solution were measured by using inductively coupled plasma optical emission spectrometer (ICP, Varian 715-ES). β-TCP scaffolds were selected as control group. Three samples from each group were tested to obtain an average value.

2.6. Stimulatory effects of the ionic products from $L_2C_4S_4$ on both osteogenesis and chondrogenesis in vitro

2.6.1. Cell culture experiments

The rabbit chondrocytes were obtained from Nanjing Medical University Nanjing Hospital. Permission of the application of the cells for *in vitro* study was authorized by the ethics commission Nanjing Medical University. Rabbit bone-marrow stem cells (rBMSCs) were provided by Cyagen Biosciences. The chondrocytes and rBMSCs were cultivated in Dulbecco's modified Eagle's medium low-glucose (DMEM) (Thermo Fisher Scientific, Grand Island, America), which included 10% fetal calf serum (Thermo Fisher Scientific), 100 U/mL penicillin and 100 μg/mL streptomycin (Thermo Fisher Scientific), at a 37 °C incubator with 5% CO_2.

2.6.2. The cell proliferation assay

The $L_2C_4S_4$ and β-TCP extracts were prepared following the protocol of International Standard Organization (ISO/EN 10993-5). The obtained raw extracts (set as 1, 200 mg/mL) of $L_2C_4S_4$ and β-TCP powders were diluted to different concentrations (1/4 (50 mg/mL), 1/8 (25 mg/mL), 1/16 (12.5 mg/mL), 1/32 (6.25 mg/mL) and 1/64 (3.125 mg/mL)). The ionic concentrations of Li, Ca and Si in the graded extracts were measured by inductively coupled plasma atomic emission spectrometry (ICP-AES, 715-ES, Varian, USA). Furthermore, different concentrations of $L_2C_4S_4$ and β-TCP extracts were used to culture rabbit chondrocytes and rBMSCs for 1, 3 and 7 days in 96-well plates. A cell counting kit-8 (CCK-8, Beyotime, China) was used to evaluate the cells proliferation in $L_2C_4S_4$ extracts [44].

2.6.3. The typical marker expression in chondrocytes and rBMSCs

After culturing with the $L_2C_4S_4$ extracts for 3 and 7 days, the typical marker expression in chondrocytes and rBMSCs was evaluated [40]. The primer sequences we used in this experiment were provided by BioSune Biotechnology Co., Ltd. (Shanghai, China). To calculate the relative value of gene expression, the value of CTR groups was set as 1. The house keeping gene, GAPDH, was used as a reference gene. All of the primer sequences were displayed in Table 1.

2.6.4. The stimulatory effect of $L_2C_4S_4$ extracts on osteogenic differentiation of rBMSCs

A calcification medium was firstly prepared for osteogenic differentiation. To prepare calcification medium, $L_2C_4S_4$ and β-TCP powders were soaked in osteogenic induction medium at 37 °C for 24 h. After culturing with the $L_2C_4S_4$ calcification medium for different times, an alkaline phosphatase colorimetric assay (ALP,

Please cite this article in press as: L. Chen, et al., 3D printing of a lithium-calcium-silicate crystal bioscaffold with dual bioactivities for osteochondral interface reconstruction, Biomaterials (2018), https://doi.org/10.1016/j.biomaterials.2018.04.005

Table 1
The primer sequences used for the RT-qPCR analysis.

Gene	Forward primer	Reverse primer
GAPDH	5-TCACCATCTTCCAGGAGCGA	5-CACAATGCCGAAGTGGTCGT
COL II	5-AACACTGCCAACGTCCAGAT	5-CTGCAGCACGGTATAGGTGA
Aggrecan	5-AGGTCGTGGTGAAAGGTGTTG	5-GTAGGTTCTCACGCCAGGGA
SOX9	5-GGTGCTCAAGGGCTACGACT	5-GGGTGGTCTTTCTTGTGCTG
N-cadh	5-TCATCTTCGTTTCCATTGGA	5-TAAGAACTCTGTAAGTTTTGG
OCN	5-CCGGGAGCAGTGTGAGCTTA	5-AGGCGGTCTTCAAGCCATACT
BMP2	5-CGCCTCAAATCCAGCTGTAAG	5-GGGCCACAATCCAGTCGTT
OPN	5-CACCATGAGAATCGCCGT	5-CGTGACTTTGGGTTTCTACGC
RUNX2	5-TCAGGCATGTCCCTCGGTAT	5-TGGCAGGTAGGTATGGTAGTG

Abcam, Cambridge, UK) and an ALP histochemical diagnostic kit (Beyotime, China) were used to study the early stage of osteogenic differentiation of rBMSCs. Furthermore, an alizarin red staining kit (Cyagen Biosciences, America) was used to study the terminal stage of osteogenic differentiation of rBMSCs. Additionally, cetylpyridinium chloride (Sinopharm Chemical Reagent Co., Ltd, China) solution (100 mM) was used to calculate the calcium deposits [45]. To fabricate a positive control group, the rBMSCs were cultured with pure osteogenic induction medium without $L_2C_4S_4$. Three samples in each group were conducted in these experiments. The images were obtained from an optics microscope (S6D, Leica, Germany).

2.7. Cell response of chondrocytes and rBMSCs in $L_2C_4S_4$ scaffolds

Steam sterilization method was used to sterilize the $L_2C_4S_4$ and β-TCP scaffolds. After chondrocytes and rBMSCs were cultured in the scaffolds for 24 h, SEM (SU8220, HITACHI, Japan) and CLSM (Leica TCS SP8, Leica Microsystems, Germany) were used to observe the cell morphology and attachment in $L_2C_4S_4$ and β-TCP scaffolds. Briefly, the cellular samples were treated with 4% paraformaldehyde, and then dehydrated in graded ethanol (30, 40, 50, 60, 70, 80, 90, 95, 100, 100, 100 v/v %) and hexamethyldisilazane (HDMS) (Sinopharm Chemical Reagent Co., Ltd, China). In order to observe the morphology and attachment of cells in a CLSM, the nuclei and cytoskeleton were stained with 4′,6-diamidino-2-phenylindole (DAPI, Sigma-Aldrich, USA) and fluorescein isothiocyanate phalloidin (FITC, Sigma-Aldrich, USA), respectively. The cells in scaffolds were observed with an Argon laser line of 488 nm (FITC channel, green) and 405 nm (DAPI channel, blue).

2.8. The in vivo regeneration of osteochondral defects for $L_2C_4S_4$ scaffolds

The guidelines for treating the New Zealand rabbits were approved by the Nanjing Medical University Ethic Committee. Three months old rabbits (2.5–3.0 Kg) were chosen to fabricate models for osteochondral defect regeneration of $L_2C_4S_4$ and β-TCP scaffolds. After induction of general anesthesia in rabbits, two cylindrical osteochondral defects were created (diameter: 4 mm, height: 5 mm) on the patellar groove, then $L_2C_4S_4$ and β-TCP scaffolds were implanted into the defect regions. Defect regions were remained untreated (blank control, $n = 6$), or transplanted with the $L_2C_4S_4$ scaffolds ($n = 6$) or β-TCP scaffolds ($n = 6$). Rabbits were treated with Penicillin for 3 days and kept singly in cages post-operation. After 8 and 12 weeks of post operation, the rabbits were sacrificed and the knee joints were collected for the following experiments. In brief, we used an intravenous overdose of pentobarbital method to sacrifice the rabbits at different time points, then the joints were photographed. Micro-CT and histological analysis were further conducted. A Micro-CT scanner (Bruker, Germany) was used to obtain the reconstruction images (2D images and 3D images) of knee joints. The relative bone volume fraction (BV/TV), bone mineral density (BMD) and trabecular numbers (Tr.N) were analyzed by using the Micro-CT scanner. Six PMMA slices from each group were treated with Safranin-O (S-O), Hematoxylin-eosin (H&E) and Toluidine blue (TB) after the gross observation and Micro-CT analysis. Images were obtained from an optic microscopy, and the cartilage defect regeneration was graded blindly by three observers in according with the international cartilage repair society (ICRS).

2.9. Statistical analysis

All data were expressed as means ± standard deviation (SD) and were analyzed using one-way ANOVA with a post hoc test. A p-value < 0.05 was considered statistically significant difference and the data were indicated with (*) for probability less than 0.05 ($p < 0.05$), (**) for $p < 0.01$, and (***) for $p < 0.001$.

3. Results

3.1. Characterization of $L_2C_4S_4$ powders

XRD patterns of $L_2C_4S_4$ powders synthesized via a sol-gel method were shown in Fig. 1A. The xerogels kept amorphous state when the calcining temperature was 500 °C. When the calcining temperature varied from 600 to 800 °C, the products mainly included $CaSiO_3$, $LiSiO_3$ and $Li_2Ca_4Si_4O_{13}$ crystal phases. High-purity $L_2C_4S_4$ powders were obtained at 940 °C, and only characteristic peaks of $Li_2Ca_4Si_4O_{13}$ powders were detected in XRD pattern (JCPDS card No. 82-1106). The thermal analysis further confirmed that the transition temperature of the amorphous xerogels was 550 °C (Fig. 1B). Fig. S1 displayed irregular morphology of pure $L_2C_4S_4$ particles, and the size of the irregular particles ranged from 5 to 20 μm.

3.2. Characterization of $L_2C_4S_4$ scaffolds

The $L_2C_4S_4$ scaffolds showed highly controlled macropore morphology, and the pore size was around 250 μm (Fig. 2A–C). High magnification SEM image displayed that the grain boundary was clearly shown on the strut surface of $L_2C_4S_4$ scaffolds (Fig. 2D). After soaked in SBF solution for 14 days, spherical apatite clusters were deposited on the surfaces of $L_2C_4S_4$ scaffolds (Fig. 2F–H). The newly formed apatite layer was composed of aggregates of nanocrystals with flake-like morphology (Fig. 2H). XRD analysis further confirmed that the newly formed crystals on the surface of $L_2C_4S_4$ scaffolds were apatite microcrystals (Fig. 2E (JCPD card No. 09-0432)). EDS analysis confirmed the existence of Ca, P and Si in the newly formed apatite crystals on the surface of $L_2C_4S_4$ scaffolds, and the Ca/P ratio of apatite was 1.57 (Fig. S2B).

3.3. Mechanical and degradation properties of $L_2C_4S_4$ scaffolds

Fig. 3(A, B) showed the $L_2C_4S_4$ scaffolds with different pore sizes and porosities. The compressive strength of $L_2C_4S_4$ scaffolds could be well controlled in the range of 15–40 MPa by varying their pore size (170–400 μm) and porosity (37–61%) (Fig. 3C). The compressive strength increased linearly with deformation of the materials (Fig. 3D).

The pH value of Tris-HCl solution in $L_2C_4S_4$ group increased with the soaking time, and the pH value was 8.48 after soaking $L_2C_4S_4$ scaffolds for 35 days, while the pH value of β-TCP group maintained in the range of 7.38–7.43 in the whole soaking span (Fig. 4A). Furthermore, $L_2C_4S_4$ scaffolds presented a sustained weight loss

Please cite this article in press as: L. Chen, et al., 3D printing of a lithium-calcium-silicate crystal bioscaffold with dual bioactivities for osteochondral interface reconstruction, Biomaterials (2018), https://doi.org/10.1016/j.biomaterials.2018.04.005

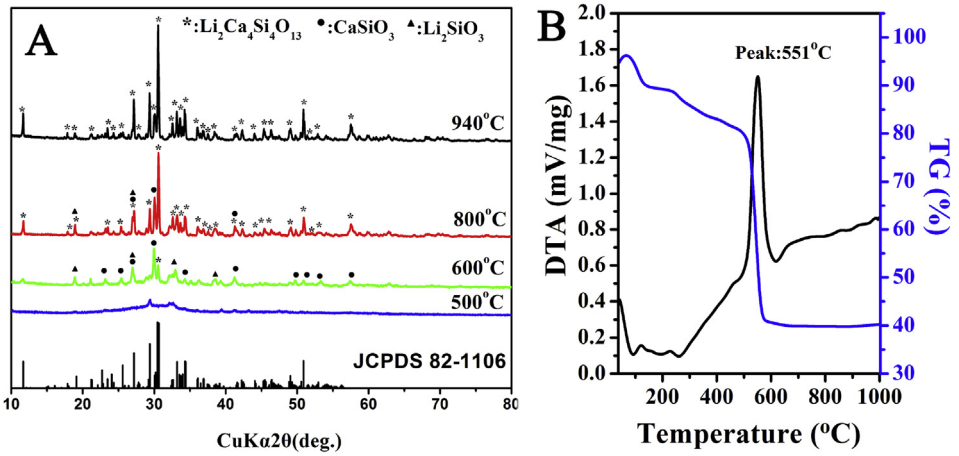

Fig. 1. Characterization of $Li_2Ca_4Si_4O_{13}$ powders. (A) XRD analysis, (B) thermal analysis. The results of XRD and thermal analysis showed that the pure phase of $Li_2Ca_4Si_4O_{13}$ powders was synthesized at 940 °C.

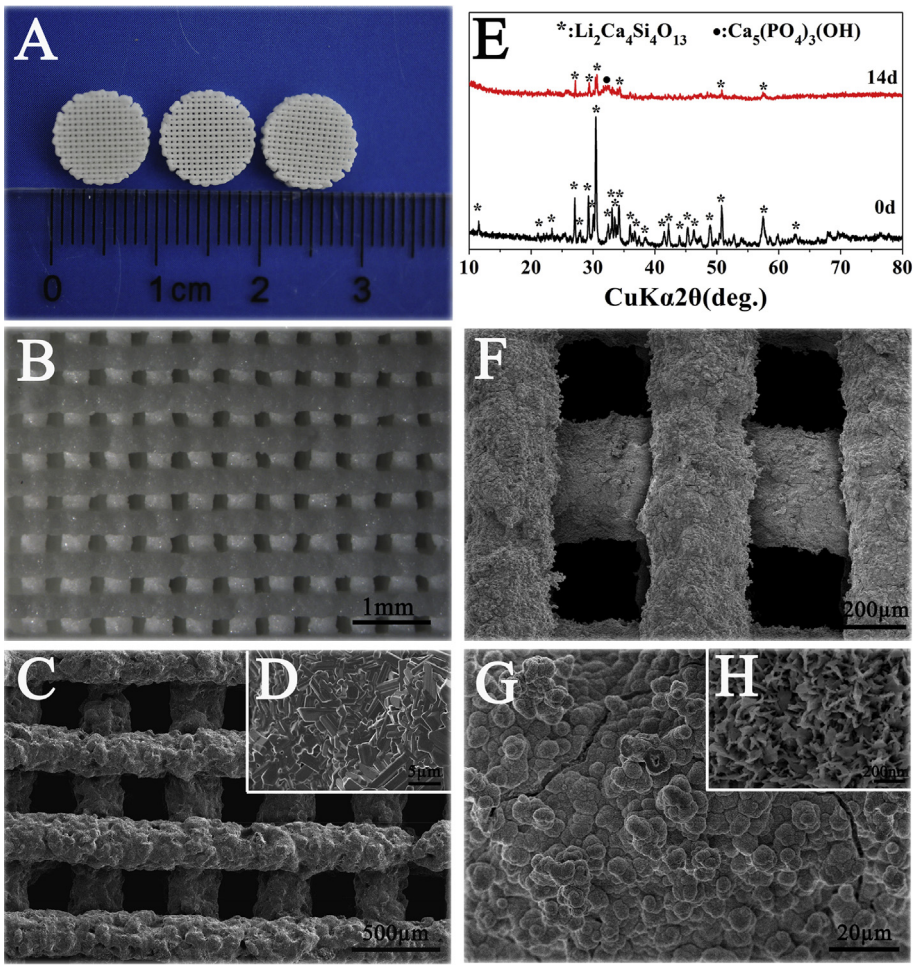

Fig. 2. Surface morphology and XRD analysis of $Li_2Ca_4Si_4O_{13}$ scaffolds. Digital photograph (A), Optical microscope image (B) and SEM images (C and D) of 3D-printed $Li_2Ca_4Si_4O_{13}$ scaffolds; The prepared porous $Li_2Ca_4Si_4O_{13}$ scaffolds possessed controlled pore size (~250 μm). XRD analysis (E) of $Li_2Ca_4Si_4O_{13}$ scaffolds before/after soaking in the simulated body fluids for 14 days; and SEM images (F–H) of $Li_2Ca_4Si_4O_{13}$ scaffolds after soaking in the simulated body fluids for 14 days. $Li_2Ca_4Si_4O_{13}$ scaffolds induced distinct apatite mineralization on their surface.

with the increase of soaking time in Tris-HCl solution (Fig. 4B). The weight loss of the $L_2C_4S_4$ scaffolds was about 27% after soaking for 35 days, which was distinctly higher than that of β-TCP scaffolds (<4%). The accumulative release amount of Ca, Si, Li, P of $L_2C_4S_4$ and β-TCP scaffolds in Tris-HCl solution at different time point was exhibited in Fig. 4C–F. The $L_2C_4S_4$ scaffolds presented distinctly

Please cite this article in press as: L. Chen, et al., 3D printing of a lithium-calcium-silicate crystal bioscaffold with dual bioactivities for osteochondral interface reconstruction, Biomaterials (2018), https://doi.org/10.1016/j.biomaterials.2018.04.005

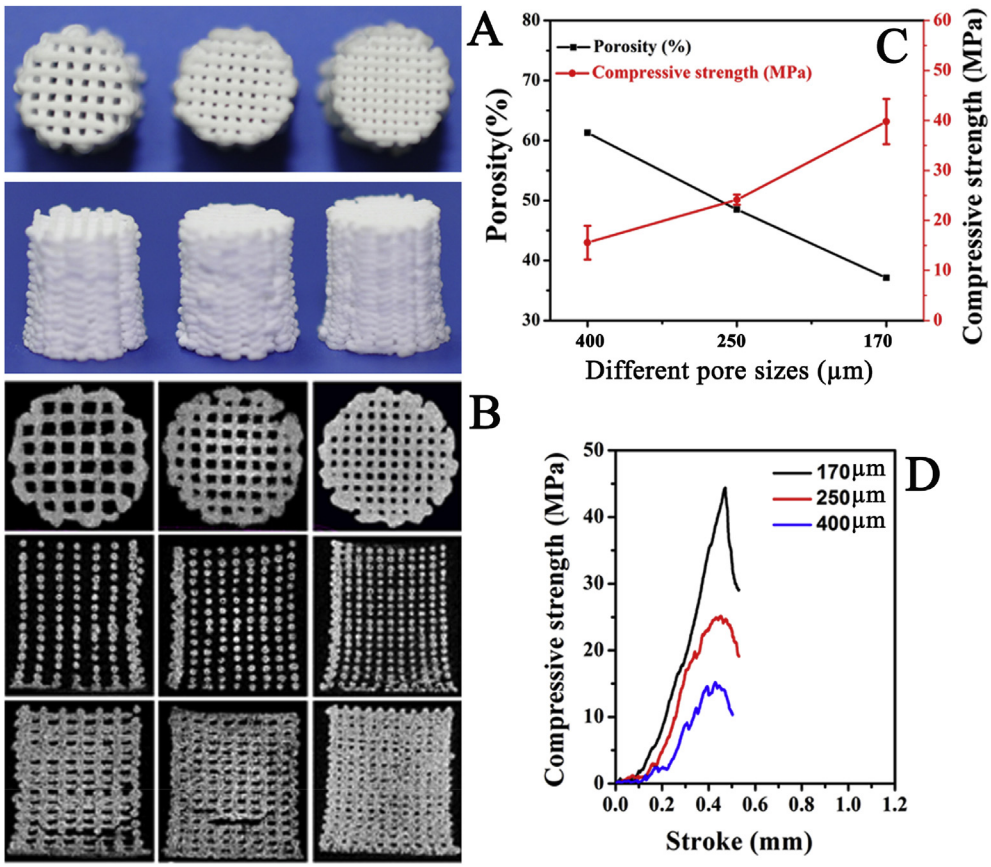

Fig. 3. Digital photographs (A) and Micro-CT images (B) of $Li_2Ca_4Si_4O_{13}$ scaffolds with different pore sizes prepared by 3D plotting for mechanical testing. (C) The effect of different pore sizes on the porosity and compressive strength of $Li_2Ca_4Si_4O_{13}$ scaffolds. (D) The curves of compressive strength with increasing scaffold deformation. The compressive strength of the $Li_2Ca_4Si_4O_{13}$ scaffolds could be effectively controlled in the range of 15–40 MPa by varying their pore size (170–400 μm) as well as porosity (37–61%).

sustained release of Ca, Si and Li, while the β-TCP scaffolds displayed slow release profile of Ca and P.

3.4. The stimulatory effects of $L_2C_4S_4$ extracts on both of chondrocytes and rBMSCs in vitro

The ionic concentrations of Li, Ca and Si in graded extracts of $L_2C_4S_4$ bioceramics were shown in Table 2. The proliferation of rBMSCs in $L_2C_4S_4$ group had no significant difference with that of β-TCP group (Fig. S3A). The proliferation of chondrocytes was distinctly elevated by $L_2C_4S_4$ extracts at the concentration range of 3.125–12.5 mg/mL over 7 days of cultured (Fig. S3B).

To further elucidate the stimulatory effect of $L_2C_4S_4$ extracts on the differentiation of both chondrocytes and rBMSCs, the expressions of chondrocytes specified genes (type II collagen, Aggrecan, N-cadh and Sox9) and osteogenic differentiation typical markers (RUNX2, OCN, type I collagen and BMP2) of rBMSCs were evaluated (Fig. 5 and Fig. S4). As compared to β-TCP group, the type II collagen and Sox9 genes were significantly enhanced by $L_2C_4S_4$ extracts at the concentration of 6.25 mg/mL (Fig. 5A and B), and the expression of Aggrecan gene distinctly increased at the concentration of 25 mg/mL over 3 days of culture (Fig. 5D). Type II collagen, Aggrecan and Sox9 expression for $L_2C_4S_4$ group was significantly enhanced at the concentration range of 6.25–25 mg/mL as compared to β-TCP group over 7 days of culture (Fig. S4A, B, D). Moreover, the N-cadh gene expression markedly up-regulated at the concentration range of 6.25–25 mg/mL as compared to β-TCP group over 3 and 7 days of culture (Fig. 5C). In addition, $L_2C_4S_4$ extracts significantly promoted RUNX2, OCN, type I collagen and BMP2 genes expression of rBMSCs at the concentration range of 6.25–25 mg/mL, as compared to β-TCP group over 3 days of culture (Fig. 5E–H). $L_2C_4S_4$ extracts obviously elevated RUNX2, OCN genes expression over 7 days of culture (Fig. S4E, F).

Fig. 6A and B and Fig. S5 displayed that $L_2C_4S_4$ extracts markedly enhanced the ALP activity and promoted the ALP expression in rBMSCs as compared to β-TCP extracts over 7 and 14 days of culture. Alizarin Red analysis was further confirmed that $L_2C_4S_4$ extracts obviously promoted the terminal mineralization of osteogenic differentiation of rBMSCs at day 21 as compared to β-TCP group (Fig. 6C and D).

3.5. The attachment of chondrocytes and rBMSCs in $L_2C_4S_4$ and β-TCP scaffolds

SEM and CLSM were used to observe the morphology and attachment of chondrocytes and rBMSCs in $L_2C_4S_4$ and β-TCP scaffolds (Fig. 7). It was found that the rBMSCs and chondrocytes spread well in both β-TCP and $L_2C_4S_4$ scaffolds, and the chondrocytes with better-defined microfilaments in $L_2C_4S_4$ scaffolds.

3.6. $L_2C_4S_4$ scaffolds stimulated the osteochondral regeneration in vivo

A rabbit osteochondral defect model was used to study the *in vivo* stimulatory effect of $L_2C_4S_4$ scaffolds for osteochondral regeneration. Digital photographs of the defects during the surgery

Please cite this article in press as: L. Chen, et al., 3D printing of a lithium-calcium-silicate crystal bioscaffold with dual bioactivities for osteochondral interface reconstruction, Biomaterials (2018), https://doi.org/10.1016/j.biomaterials.2018.04.005

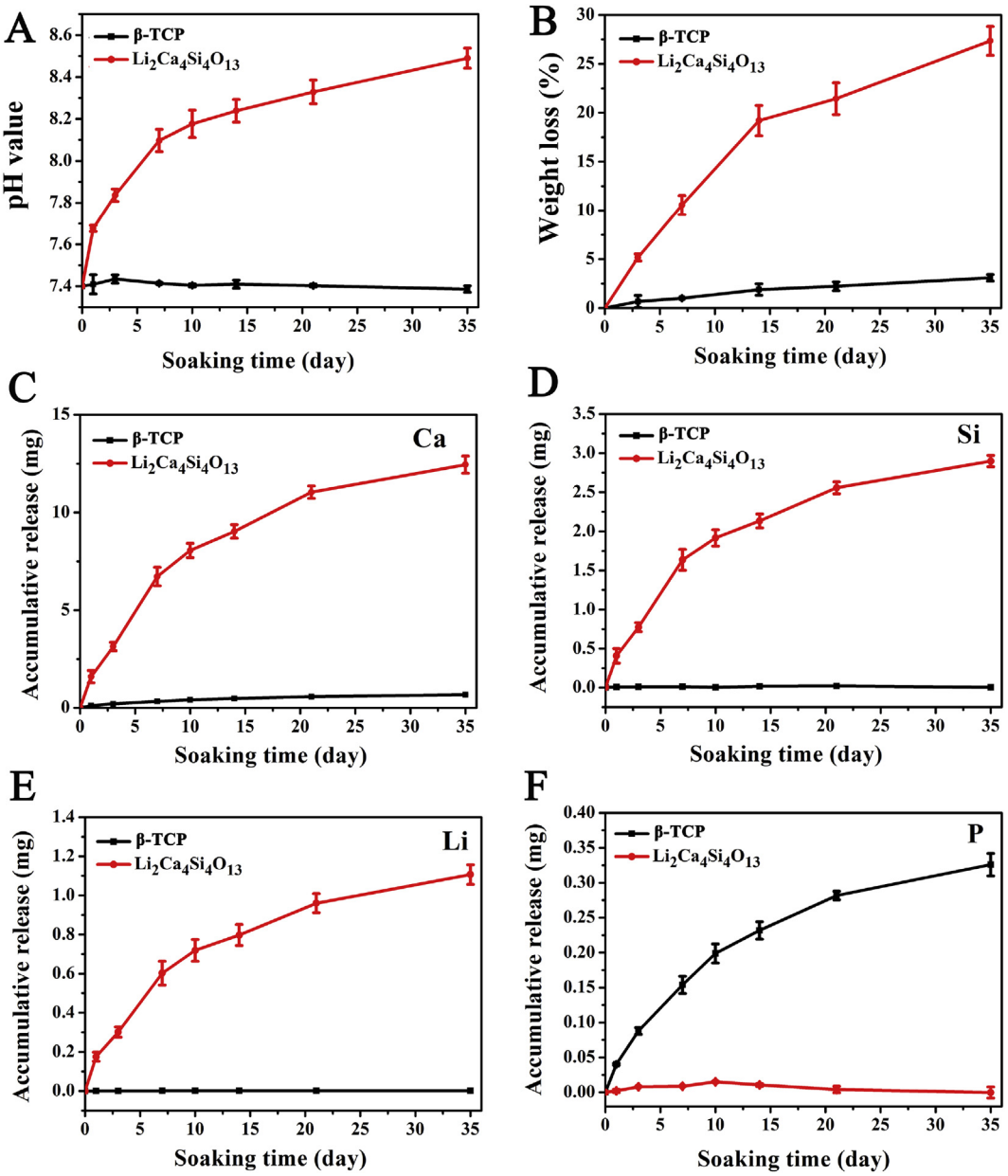

Fig. 4. (A) The pH change of Tris-HCl buffer after soaking the scaffolds. (B) The weight loss of $Li_2Ca_4Si_4O_{13}$ and β-TCP scaffolds after soaking in Tris-HCl buffer for different time periods. The accumulative release amount of Ca (C), Si (D), Li (E), P (F) of $Li_2Ca_4Si_4O_{13}$ and β-TCP scaffolds in Tris-HCl solution at different time point. The $Li_2Ca_4Si_4O_{13}$ scaffolds presented a sustained ion release and weight loss with the increase of the soaking time in Tris-HCl solution (n = 3).

Table 2
The ionic concentration of Li, Ca, Si and P in $Li_2Ca_4Si_4O_{13}$ and β-TCP extracts.

Ionic Con.	Powder extract concentrations (mg L^{-1})						
	0	6.25		12.5		25	
	CTR	β-TCP	$Li_2Ca_4Si_4O_{13}$	β-TCP	$Li_2Ca_4Si_4O_{13}$	β-TCP	$Li_2Ca_4Si_4O_{13}$
Li	0.0	0.0	3.9	0.0	7.2	0.0	14.9
Ca	65.3	64.8	64.3	63.6	62.4	60.6	60.9
Si	0.3	0.3	13.8	0.4	24.5	0.4	51.4
P	29.6	28.7	28.8	27.9	28.1	26.0	25.9

were shown in Fig. 8a–c. The macro-photograph and Micro-CT analysis of knees collected at week 8 and 12 were shown in Fig. 8. There was no inflammation happened in all of the collected knee joints. Well-integrated tissue was found in β-TCP and $Li_2Ca_4Si_4O_{13}$ groups, while there was large residual void space in the CTR group at 8 weeks (Fig. 8A_1-C_1). At week 12, the defects in $L_2C_4S_4$ group were filled with glossy white and well integrated tissues, which had no distinct difference between CTR and β-TCP

Please cite this article in press as: L. Chen, et al., 3D printing of a lithium-calcium-silicate crystal bioscaffold with dual bioactivities for osteochondral interface reconstruction, Biomaterials (2018), https://doi.org/10.1016/j.biomaterials.2018.04.005

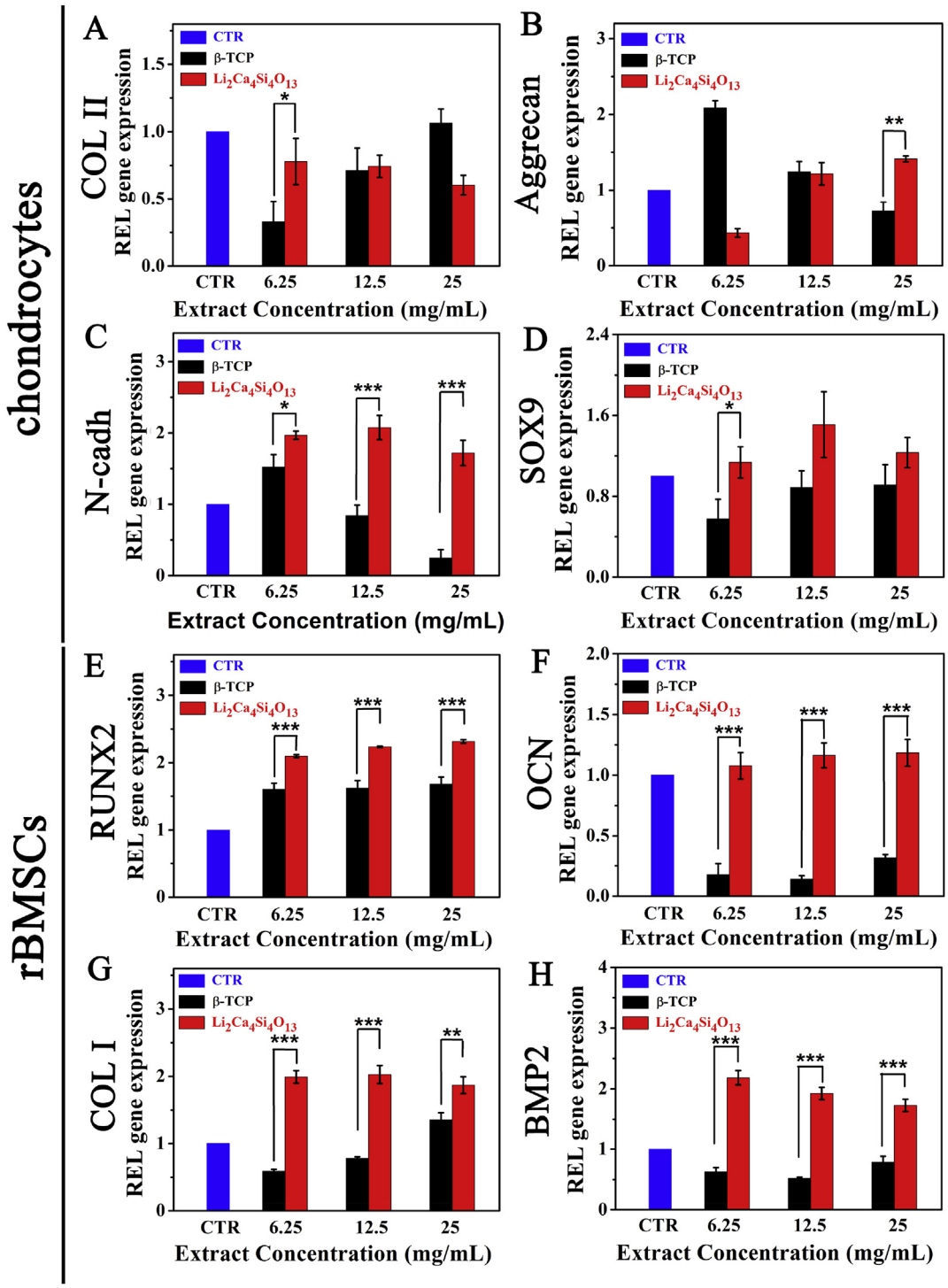

Fig. 5. The relative genes expression in chondrocytes (A–D) and rBMSCs (E–H) cultured with the extracts of β-TCP and $Li_2Ca_4Si_4O_{13}$ for 3 days. The gene expressions of type II collagen (A), Aggrecan (B), N-cadh (C) and Sox9 (D), in chondrocytes after co-culturing with the extracts respectively. The gene expressions of Runx2 (E), OCN (F), type I collagen (G) and BMP2 (H) in rBMSCs post co-culturing with the extracts, respectively. As compared to β-TCP group, the type II collagen and Sox9 genes were significantly enhanced by $Li_2Ca_4Si_4O_{13}$ extracts at the concentration of 6.25 mg/mL, and the expression of Aggrecan gene distinctly increased at the concentration of 25 mg/mL. Moreover, the N-cadh gene expression markedly up-regulated at the concentration range of 6.25–25 mg/mL as compared to β-TCP group. In addition, $Li_2Ca_4Si_4O_{13}$ extracts significantly promoted RUNX2, OCN, BMP2 and type I collagen gene expressions at the concentration range of 6.25–25 mg/mL as compared to β-TCP group (*$p < 0.05$, **$p < 0.01$, ***$p < 0.001$) ($n = 6$).

groups in appearance. The Micro-CT analysis showed that there was considerable amount of calcified tissue in $L_2C_4S_4$ group, while the CTR groups were noted to have large residual void spaces at week 8 and 12, and the amount of calcified tissue in TCP groups was lower than $L_2C_4S_4$, but higher than CTR groups (Fig. 8A_2-F_4). Moreover, the ICRS score of $L_2C_4S_4$ group was significantly enhanced as compared to CTR and β-TCP groups at week 12 (Fig. S7D). In addition, the BV/TV, BMD and Tr.N exhibited increasing profile in $L_2C_4S_4$ group as compared to CTR and β-TCP groups at week 8 and 12 (Fig. S7A-C).

To further investigate the efficacy of $L_2C_4S_4$ scaffolds for cartilage

Please cite this article in press as: L. Chen, et al., 3D printing of a lithium-calcium-silicate crystal bioscaffold with dual bioactivities for osteochondral interface reconstruction, Biomaterials (2018), https://doi.org/10.1016/j.biomaterials.2018.04.005

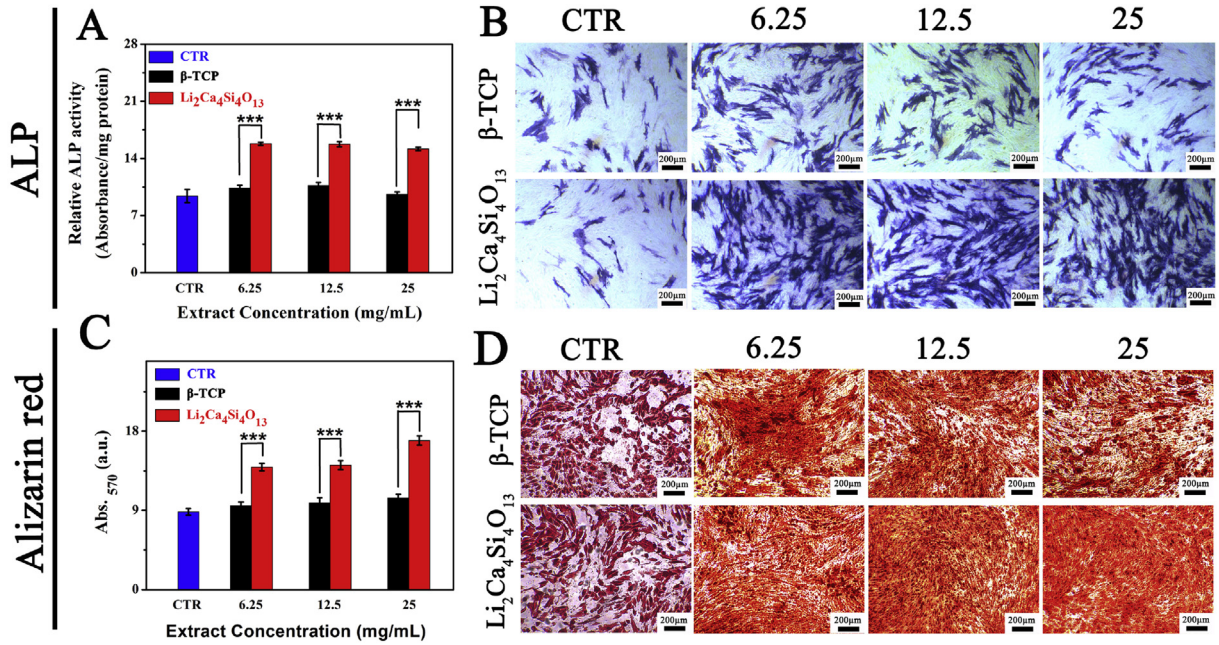

Fig. 6. The osteogenic differentiation of rBMSCs. The ALP activity of rBMSCs cultured with the extracts of β-TCP and $Li_2Ca_4Si_4O_{13}$ for 14 days, (A) ALP activity, (B) ALP staining images; The Alizarin red analysis of rBMSCs cultured with the extracts of β-TCP and $Li_2Ca_4Si_4O_{13}$ for 21 days, (C) Alizarin red quantification, and (D) Alizarin red staining images. As compared to β-TCP, $Li_2Ca_4Si_4O_{13}$ distinctly promoted the osteogenic differentiation of rBMSCs (***$p < 0.001$) ($n = 6$). (For interpretation of the references to color in this figure legend, the reader is referred to the Web version of this article.)

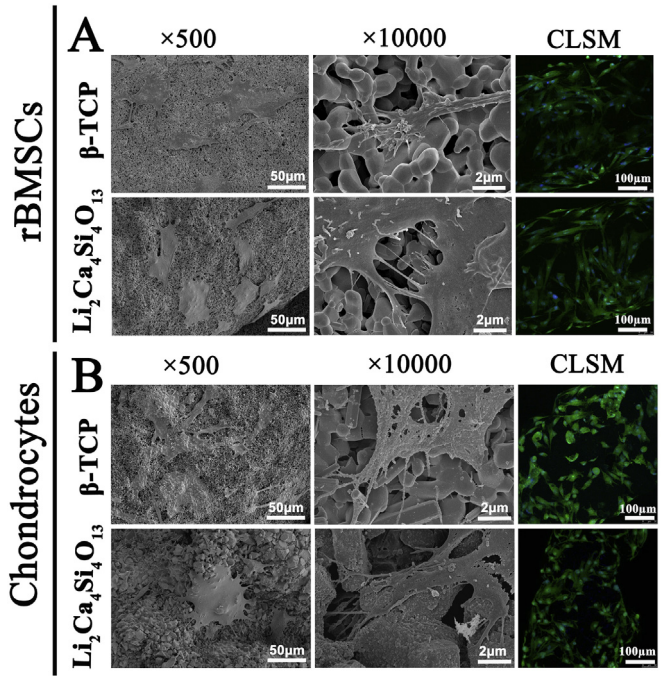

Fig. 7. SEM and CLSM images of rBMSCs (A) and chondrocytes (B) cultured in β-TCP and $Li_2Ca_4Si_4O_{13}$ scaffolds for 1 day. The rBMSCs and chondrocytes spread well on both β-TCP and $Li_2Ca_4Si_4O_{13}$ scaffolds, and the chondrocytes with better-defined microfilaments in $Li_2Ca_4Si_4O_{13}$ scaffolds.

and subchondral bone reconstruction, the histological analysis of S-O, H&E and TB staining was conducted (Fig. 9 and Fig. S6). H&E staining showed that residual void space and fibrous tissue were found in CTR and β-TCP groups at week 8 and 12, while well-integrated tissue was filled in the defect of $L_2C_4S_4$ group at week 12 (Fig. S6A_1-F_1). TB staining displayed that there was considerable amount of glycosaminoglycans (GAGs) in $L_2C_4S_4$ group, which was markedly enhanced as compared to CTR and β-TCP groups (Fig. S6A_2-F_2). S-O staining showed that $L_2C_4S_4$ group possessed rich GAGs, while β-TCP group exhibited a slightly enhanced GAGs compared to CTR group (Fig. 9). Moreover, the defect center of CTR group remained discontinuous at week 8, and β-TCP group was filled with fibrous tissue and neo-bony tissue, while $L_2C_4S_4$ group was fully covered with neo-hyaline cartilage and neo-bone tissues at both of week 8 and 12.

4. Discussion

In this study, we successfully synthesized a pure-phase $L_2C_4S_4$ bioceramic by a sol-gel method. $L_2C_4S_4$ is a Li, Ca and Si-containing ternary compound [46]. It is known that the synthesis of multi-components crystals with high purity is of great challenging. Previously, $L_2C_4S_4$ compound was synthesized via a solid state reaction method, in which the synthetic steps were usually required to calcine above 1000 °C at least 20 days with 2 or 3 times melting and quenching operations, which was quite complicated and time-consuming [42]. In this study, highly pure $L_2C_4S_4$ crystals were synthesized via a simple sol-gel method. Sol-gel method is a wet-chemical technique used for the fabrication of both glassy and ceramic materials. Comparing with traditional solid state reaction method, the used sol-gel approach in this study could well control their chemical composition, due to the following advantages, such as simple operation and low reaction temperature. Furthermore, the size of the $L_2C_4S_4$ particles could be well controlled range from 5 to 20 μm, which was obviously smaller than the $L_2C_4S_4$ crystals prepared by solid state reaction method. Our results indicated that sol-gel method represents an advanced strategy to synthesize $L_2C_4S_4$ crystals with high purity.

The second important novelty is that we successfully prepared highly uniform $L_2C_4S_4$ scaffolds with excellent mechanical strength via 3D printing, and the mechanical strength can be well modulated

Please cite this article in press as: L. Chen, et al., 3D printing of a lithium-calcium-silicate crystal bioscaffold with dual bioactivities for osteochondral interface reconstruction, Biomaterials (2018), https://doi.org/10.1016/j.biomaterials.2018.04.005

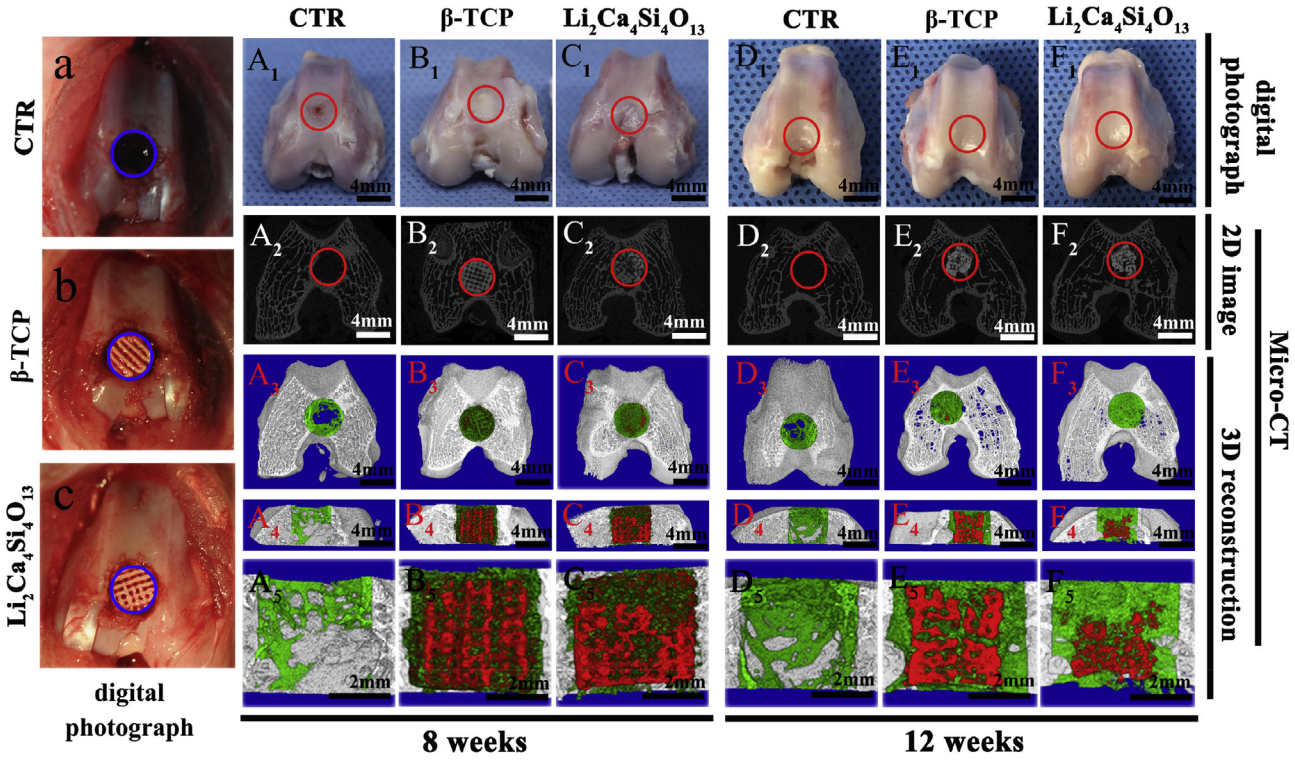

Fig. 8. Digital photographs of the defects in the three experimental groups during the surgery (a–c). Digital photographs and Micro-CT imaging analysis of the defects in the three groups at 8 and 12 weeks of post-surgery (A–F). Macro-photographs showed the defects in the control group and the other two experimental groups (A_1 and D_1: blank control without scaffolds, B_1 and E_1: pure β-TCP scaffolds, C_1 and F_1: $Li_2Ca_4Si_4O_{13}$ scaffolds) at 8 and 12 weeks of post-surgery. A_2-C_2 and D_2-F_2 showed 2D projection images of the three experimental groups at week 8 and 12, respectively. A_3-C_3 and D_3-F_3 showed the transverse view of 3D reconstruction images of the three experimental groups at week 8 and 12, respectively. A_4-C_4 and D_4-F_4 showed the sagittal view of 3D reconstruction images of the three experimental groups at week 8 and 12, respectively. A_5-F_5 were the high-magnification images of A_4-F_4. In 3D reconstruction images, the off-white color, green color and red color stand for primary bone, new bone and scaffold, respectively. Digital photographs and Micro-CT analysis of the defect space demonstrated that the regenerated bone in $Li_2Ca_4Si_4O_{13}$ groups significantly enhanced as compared to CTR and β-TCP groups at both of 8 and 12 weeks. (For interpretation of the references to color in this figure legend, the reader is referred to the Web version of this article.)

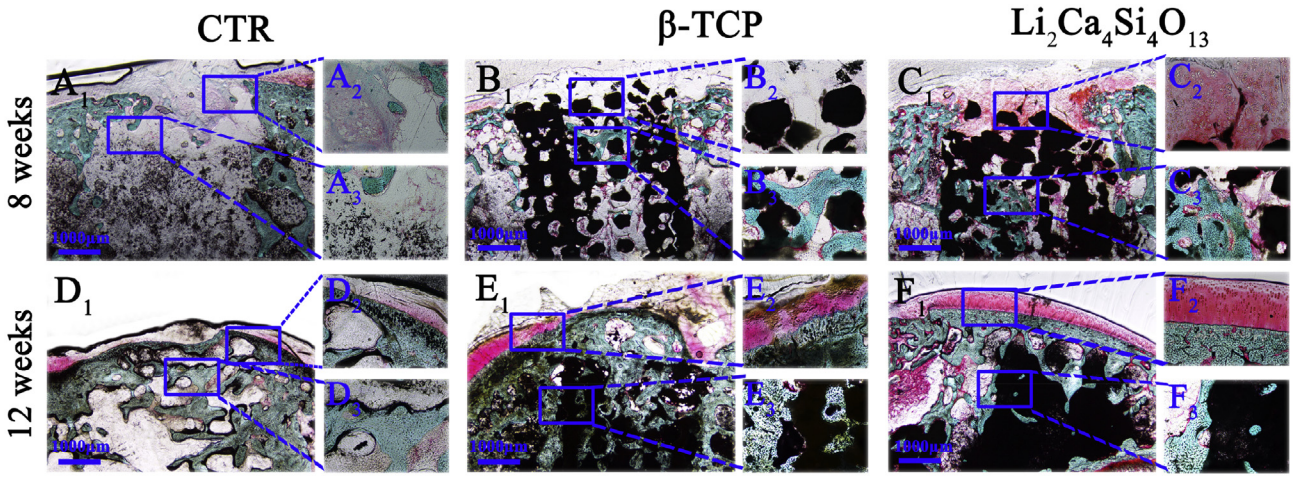

Fig. 9. The regeneration quality of cartilage and subchondral bone *in vivo* at 8 and 12 weeks of post-surgery. (A_1-F_3) Safranin-O/Fast Green staining at 8 weeks (A_1-C_3) and 12 weeks (D_1-F_3) of post-surgery. $A_{1\text{-}3}$ and $D_{1\text{-}3}$: CTR group, $B_{1\text{-}3}$ and $E_{1\text{-}3}$: β-TCP group, $C_{1\text{-}3}$ and $D_{1\text{-}3}$: $Li_2Ca_4Si_4O_{13}$ group. The black color, blue color and red color stand for scaffold, bone and cartilage, respectively. The Safranin-O/Fast Green staining demonstrated that $Li_2Ca_4Si_4O_{13}$ group possessed considerable amount of hyaline cartilage-like tissue as compared to the other two experimental groups at week 12. (For interpretation of the references to color in this figure legend, the reader is referred to the Web version of this article.)

by controlling macropore sizes of $L_2C_4S_4$ scaffolds. It is well known that scaffolds with an excessively high porosity may have poor mechanical properties and sacrifice their load-bearing ability [47]. Previous studies have shown that the compressive strength of 3D-printed bioceramic or bioglass scaffolds (such as $Ca_3(PO_4)_2$, $CaSiO_3$, $Sr_5(PO_4)_2SiO_4$, Sr-MBG) could reach 4–8 MPa when the porosity was 60% [31,44,48–50]. Interestingly, in our study the compressive strength of the 3D-printed $L_2C_4S_4$ scaffolds was up to 15 MPa, which was around 2–3 times higher than that of other 3D-printed bioceramic scaffolds. The compressive strength of the 3D-printed

Please cite this article in press as: L. Chen, et al., 3D printing of a lithium-calcium-silicate crystal bioscaffold with dual bioactivities for osteochondral interface reconstruction, Biomaterials (2018), https://doi.org/10.1016/j.biomaterials.2018.04.005

$L_2C_4S_4$ scaffolds was comparable with that of cancellous bone (2–12 MPa), suggesting that it is sufficient for providing the initial structure and stability for subchondral bone tissue formation [51]. Except for the mechanical properties, the pore size and porosity of scaffolds are important factors for bone regeneration. It was reported that bioactive scaffolds play an important role in influencing the biological response of tissue cells and tissue formation [7]. Previous studies indicated that pores with sizes over 100 μm allowed cells migration and transportation, and macropores (>300 μm) provided space for new bone formation and bone ingrowth [52–54]. In our study, the pore size of $L_2C_4S_4$ scaffolds was within the range of 170–400 μm. The 3D-printed $L_2C_4S_4$ scaffolds possessed the higher connectivity and controlled porosity (37–61%), which may have higher efficiency for nutrient exchange, which has better osteogenesis effects for bone regeneration. Additionally, the weight loss of $L_2C_4S_4$ scaffolds distinctly elevated, which was higher than that of conventional β-TCP scaffolds, demonstrating that the $L_2C_4S_4$ scaffolds possess favorable biodegradability. Hence, the $L_2C_4S_4$ scaffolds with excellent mechanical strength and favorable biodegradability may be suitable for the young patients who need quick degradation of biomaterials for quickly improving tissue reconstruction.

The most distinct novelty of the study is dual bioactivities of $L_2C_4S_4$ scaffolds. The dual bioactivities include two aspects. On the one hand, the ionic products of $L_2C_4S_4$ bioceramics at the concentration range of 6.25–25 mg/mL not only promoted cartilage maturation, but also stimulated osteogenic differentiation *in vitro*; on the other hand, $L_2C_4S_4$ scaffolds significantly accelerated cartilage regeneration as well as promoted subchondral bone reconstruction *in vivo*. The scaffolds were degradable, but the accumulative release of Li ions from scaffolds was no more than 1.2 mg after soaking for 35 days, which would have no distinct cytotoxicity effect in such a low release amount. In addition, we have studied the possible toxicity caused by Li ions in this study. The results of the CCK8 experiments demonstrated that Li did not cause adverse effects on rBMSCs and chondrocytes within the certain concentration range (0–14.85 mg/L). Furthermore, the Micro-CT and histological analysis indicated that the Li ions released from L2C4S4 scaffolds did not cause acute or chronic poisoning within the 12 weeks of *in vivo* implantation.

In the aspect of chondrogenesis bioactivity, the Sox9 (transcripts promoter region) production in chondrocytes was significantly enhanced by $L_2C_4S_4$ extracts, following by up-regulating type II collagen, Aggrecan and N-cadh genes. Previous studies indicated that Sox9, a transcripts promoter region, could stimulate type II collagen, Aggrecan and N-cadh genes expression [55]. The enhanced expression of type II collagen, Aggrecan and N-cadh followed by Sox9 production could support energy for matrix synthesis for cartilage repair [56–58]. Consequently, $L_2C_4S_4$ bioceramic significantly stimulated chondrocytes maturation and promoted cartilage regeneration via promoting Sox9 and type II collagen expression, as well as elevating Aggrecan and N-cadh expression to support energy for matrix synthesis and cartilage reconstruction.

In the aspect of osteogenesis bioactivity, $L_2C_4S_4$ scaffolds induced significant apatite mineralization, and the ionic products of $L_2C_4S_4$ bioceramic significantly promoted the osteogenic differentiation of rBMSCs *in vitro*, also the $L_2C_4S_4$ scaffolds obviously stimulated the reconstruction of subchondral bone *in vivo*. Previous evidences showed, SiO_4^{4-} groups in silicate-based biomaterials are of great importance to induce apatite mineralization [59–61]. SiO_4^{4-} groups formed Si-rich layer, which provided the nuclear sites for apatite mineralization. In this study, the structure of $L_2C_4S_4$ was composed of two types of silicate anions: isolated (SiO_4^{4-}) tetrahedral and infinite chains ($Si_3O_9^{6-}$) along the [001] axis with three tetrahedral in the repeat unit [42]. Hence, SiO_4^{4-} groups might form Si-rich layer on the surface of $L_2C_4S_4$ scaffolds and provided the nuclear sites for apatite mineralization. Previous studies demonstrated that apatite mineralization on the surface of biomaterials played an important role in improving osteoblast growth and differentiation, as well as enhanced the *in vivo* bone-forming stimulation ability [43,62–65]. In our study, it was found that the expression of bone-related genes (RUNX2, OCN, type I collagen and BMP2) distinctly elevated after culturing with $L_2C_4S_4$ extracts at the concentration range of 6.25–25 mg/mL. Moreover, the ALP activity and mineralization, which stand for the early and terminal term of osteogenic differentiation of rBMSCs, were distinctly enhanced in $L_2C_4S_4$ group as compared to the other experimental groups. Previously, RUNX2 could stimulate the osteogenic differentiation of rBMSCs via promoting the type I collagen, OCN, BMP2 and ALP expression [66,67]. Hence, it is reasonable to speculate that $L_2C_4S_4$ bioceramics promoted the osteogenic differentiation of rBMSCs and stimulated subchondral bone regeneration through enhancing RUNX2 expression and further inducing the early and later mineralization of rBMSCs for subchondral bone reconstruction. The potential mechanism may be related to the synergistic effect of released Li, Ca and Si ions as well as the uniform macropores of scaffolds.

Recently, biphasic and triphasic scaffolds have been developed for mimicking the microstructure of cartilage and subchondral bone. However, it remains a great challenge to regenerate both of cartilage and subchondral bone at the same time, due to the insufficient bioactivities of multi-layer scaffolds. Furthermore, some obvious drawbacks, such as inadequate bonding force between two different layers and complex preparation processes, existed in multi-layer scaffolds [13,14]. In this study, a single type of $L_2C_4S_4$ scaffolds with dual bioactivities were successfully fabricated. $L_2C_4S_4$ scaffolds with monophasic structure could avert the delamination issues, which is superior to multi-layered scaffolds. $L_2C_4S_4$ scaffolds with the excellent mechanical properties could support subchondral bone regeneration. According to the different requirements of patients, the compressive strength and degradation rate of $L_2C_4S_4$ scaffolds could be well controlled through modulating the porosity of $L_2C_4S_4$ scaffolds. Furthermore, the Li and Si ions released from the monophasic $L_2C_4S_4$ scaffolds could stimulate both of cartilage and subchondral bone regeneration simultaneously. Consequently, $L_2C_4S_4$ scaffolds possessed bi-lineage bioactivities for regeneration of both cartilage and subchondral bone, which represents a smart strategy for osteochondral defect regeneration.

5. Conclusion

In this study, pure $L_2C_4S_4$ crystals were successfully synthesized by a sol-gel method, and $L_2C_4S_4$ scaffolds with highly uniform macropore structure were fabricated via 3D-printing technique. The compressive strength of $L_2C_4S_4$ scaffolds could be effectively controlled in the range of 15–40 MPa by varying their pore size (170–400 μm), which is higher than traditional bioceramic and polymer scaffolds. The 3D-printed $L_2C_4S_4$ scaffolds had distinct apatite-mineralization ability, which benefited for the attachment of chondrocytes and rBMSCs. In addition, the $L_2C_4S_4$ extracts at the concentration range of 6.25–25 mg/mL distinctly stimulated the maturation of chondrocytes and promoted the osteogenic differentiation of rBMSCs *in vitro*, and $L_2C_4S_4$ scaffolds promoted the regeneration of both cartilage and subchondral bone *in vivo*. Our study suggests that $L_2C_4S_4$ scaffolds possess dual bioactivities and can biologically fulfill the requirements of regeneration of both cartilage and subchondral bone, which represents a feasible strategy for osteochondral reconstruction.

Please cite this article in press as: L. Chen, et al., 3D printing of a lithium-calcium-silicate crystal bioscaffold with dual bioactivities for osteochondral interface reconstruction, Biomaterials (2018), https://doi.org/10.1016/j.biomaterials.2018.04.005

Acknowledgements

This work was supported by the National Key Research and Development Program of China (2016YFB0700803), the Natural Science Foundation of China (5171101275, 81771989, 81601612), Key Research Program of Frontier Sciences CAS (QYZDB-SSW-SYS027) and Science and Technology Commission of Shanghai Municipality (17441903700, 16DZ2260603, 17540712300) and Key Research Program of Science & Technology Support Program of Jiangsu Province (BE2016763).

Appendix A. Supplementary data

Supplementary data related to this article can be found at https://doi.org/10.1016/j.biomaterials.2018.04.005.

References

[1] E.B. Hunziker, Articular cartilage repair: basic science and clinical progress. A review of the current status and prospects, Osteoarthr. Cartil. 10 (6) (2002) 432–463.
[2] B.S. Dhinsa, A.B. Adesida, Current clinical therapies for cartilage repair, their limitation and the role of stem cells, Curr. Stem Cell Res. Ther. 7 (2) (2012) 143–148.
[3] H. Madry, C.N. van Dijk, M. Mueller-Gerbl, The basic science of the subchondral bone, Knee Surg. Sports Traumatol. 18 (4) (2010) 419–433.
[4] T. Funck-Brentano, M. Cohen-Solal, Crosstalk between cartilage and bone: when bone cytokines matter, Cytokine Growth Factor Rev. 22 (2) (2011) 91–97.
[5] R.J. Lories, F.P. Luyten, The bone-cartilage unit in osteoarthritis, Nat. Rev. Rheumatol. 7 (1) (2011) 43–49.
[6] E.B. Hunziker, The elusive path to cartilage regeneration, Adv. Mater. 21 (32–33) (2009) 3419–3424.
[7] D.W. Hutmacher, Scaffolds in tissue engineering bone and cartilage, Biomaterials 21 (24) (2000) 2529–2543.
[8] T.G. Kim, H. Shin, D.W. Lim, Biomimetic scaffolds for tissue engineering, Adv. Funct. Mater. 22 (12) (2012) 2446–2468.
[9] S.-J. Seo, C. Mahapatra, R.K. Singh, J.C. Knowles, H.-W. Kim, Strategies for osteochondral repair: focus on scaffolds, J. Tissue Eng. 5 (2014), 2041731414541850–2041731414541850.
[10] I. Martin, S. Miot, A. Barbero, M. Jakob, D. Wendt, Osteochondral tissue engineering, J. Biomech. 40 (4) (2007) 750–765.
[11] P. Nooeaid, V. Salih, J.P. Beier, A.R. Boccaccini, Osteochondral tissue engineering: scaffolds, stem cells and applications, J. Cell Mol. Med. 16 (10) (2012) 2247–2270.
[12] K. Shimomura, Y. Moriguchi, C.D. Murawski, H. Yoshikawa, N. Nakamura, Osteochondral tissue engineering with biphasic scaffold: current strategies and techniques, Tissue Eng. Part B 20 (5) (2014) 468–476.
[13] R.A. Kandel, M. Grynpas, R. Pilliar, J. Lee, J. Wang, S. Waldman, P. Zalzal, M. Hurtig, C.B.S.T. Team, Repair of osteochondral defects with biphasic cartilage-calcium polyphosphate constructs in a Sheep model, Biomaterials 27 (22) (2006) 4120–4131.
[14] B. Marquass, J.S. Somerson, P. Hepp, T. Aigner, S. Schwan, A. Bader, C. Josten, M. Zscharnack, R.M. Schulz, A novel MSC-seeded triphasic construct for the repair of osteochondral defects, J. Orthop. Res. 28 (12) (2010) 1586–1599.
[15] J. Chen, H. Chen, P. Li, H. Diao, S. Zhu, L. Dong, R. Wang, T. Guo, J. Zhao, J. Zhang, Simultaneous regeneration of articular cartilage and subchondral bone in vivo using MSCs induced by a spatially controlled gene delivery system in bilayered integrated scaffolds, Biomaterials 32 (21) (2011) 4793–4805.
[16] A.K. Lynn, S.M. Best, R.E. Cameron, B.A. Harley, I.V. Yannas, L.J. Gibson, W. Bonfield, Design of a multiphase osteochondral scaffold. I. Control of chemical composition, J. Biomed. Mater. Res. Part A 92A (3) (2010) 1057–1065.
[17] T. Novak, B. Seelbinder, C.M. Twitchell, S.L. Voytik-Harbin, C.P. Neu, Dissociated and reconstituted cartilage microparticles in densified collagen induce local hMSC differentiation, Adv. Funct. Mater. 26 (30) (2016) 5427–5436.
[18] I.C. Liao, F.T. Moutos, B.T. Estes, X.H. Zhao, F. Guilak, Composite three-dimensional woven scaffolds with interpenetrating network hydrogels to create functional synthetic articular cartilage, Adv. Funct. Mater. 23 (47) (2013) 5833–5839.
[19] R. Chen, J. Wang, C.S. Liu, Biomaterials act as enhancers of growth factors in bone regeneration, Adv. Funct. Mater. 26 (48) (2016) 8810–8823.
[20] R.M. Jeuken, A.K. Roth, R. Peters, C.C. van Donkelaar, J.C. Thies, L.W. van Rhijn, P.J. Emans, Polymers in cartilage defect repair of the knee: current status and future prospects, Polymers 8 (6) (2016).
[21] A.-M. Yousefi, M.E. Hoque, R.G.S.V. Prasad, N. Uth, Current strategies in multiphasic scaffold design for osteochondral tissue engineering: a review, J. Biomed. Mater. Res. Part A 103 (7) (2015) 2460–2481.
[22] C.T. Wu, J. Chang, Silicate bioceramics for bone tissue regeneration, J. Inorg. Mater. 28 (1) (2013) 29–39.
[23] K. Schwarz, D.B. Milne, Growth-promoting effects of silicon in rats, Nature 239 (5371) (1972), 333-&.
[24] E.M. Carlisle, Silicon: a possible factor in bone calcification, Science 167 (3916) (1970) 279–280.
[25] M. Bohner, Silicon-substituted calcium phosphates - a critical view, Biomaterials 30 (32) (2009) 6403–6406.
[26] C.T. Wu, J. Chang, A review of bioactive silicate ceramics, Biomed. Mater. 8 (3) (2013).
[27] S. Sweeney, A. Adamcakova-Dodd, P.S. Thorne, J.G. Assouline, Biocompatibility of multi-imaging engineered mesoporous silica nanoparticles: in vitro and adult and fetal in vivo studies, J. Biomed. Nanotechnol. 13 (5) (2017) 544–558.
[28] Y. Huang, X. Jin, X. Zhang, H. Sun, J. Tu, T. Tang, J. Chang, K. Dai, In vitro and in vivo evaluation of akermanite bioceramics for bone regeneration, Biomaterials 30 (28) (2009) 5041–5048.
[29] H. Gu, F. Guo, X. Zhou, L. Gong, Y. Zhang, W. Zhai, L. Chen, L. Cen, S. Yin, J. Chang, L. Cui, The stimulation of osteogenic differentiation of human adipose-derived stem cells by ionic products from akermanite dissolution via activation of the ERK pathway, Biomaterials 32 (29) (2011) 7023–7033.
[30] W.Y. Zhai, H.X. Lu, C.T. Wu, L. Chen, X.T. Lin, K. Naoki, G.P. Chen, J. Chang, Stimulatory effects of the ionic products from Ca-Mg-Si bioceramics on both osteogenesis and angiogenesis in vitro, Acta Biomater. 9 (8) (2013) 8004–8014.
[31] S.C. Zhao, J.H. Zhang, M. Zhu, Y.D. Zhang, Z.T. Liu, C.L. Tao, Y.F. Zhu, C.Q. Zhang, Three-dimensional printed strontium-containing mesoporous bioactive glass scaffolds for repairing rat critical-sized calvarial defects, Acta Biomater. 12 (2015) 270–280.
[32] M.-H. Wang, H.-B. Zhong, Y.-C. Fan, T. Chen, Spark plasma sintering of bioactive Ca2MgSi2O7 ceramics, J. Inorg. Mater. 32 (8) (2017) 825–830.
[33] M.R.V.B. Calomme, D. A, Supplementation of calves with stabilized orthosilicic acid, Biol. Trace Elem. Res. 56 (2) (1997) 153–165.
[34] F.H. Nielsen, R. Poellot, Dietary silicon affects bone turnover differently in ovariectomized and sham-operated growing rats, J. Trace Elem. Exp. Med. 17 (3) (2004) 137–149.
[35] R.S.B. Williams, A.J. Harwood, Lithium therapy and signal transduction, Trends Pharmacol. Sci. 21 (2) (2000) 61–64.
[36] P. Clement-Lacroix, M.R. Ai, F. Morvan, S. Roman-Roman, B. Vayssiere, C. Belleville, K. Estrera, M.L. Warman, R. Baron, G. Rawadi, Lrp5-independent activation of Wnt signaling by lithium chloride increases bone formation and bone mass in mice, Proc. Natl. Acad. Sci. U. S. A 102 (48) (2005) 17406–17411.
[37] W. Hui, G.J. Litherland, M. Jefferson, M.J. Barter, M.S. Elias, T.E. Cawston, A.D. Rowan, D.A. Young, Lithium protects cartilage from cytokine-mediated degradation by reducing collagen-degrading MMP production via inhibition of the P38 mitogen-activated protein kinase pathway, Rheumatology (Oxford) 49 (11) (2010) 2043–2053.
[38] T. Minashima, Y. Zhang, Y. Lee, T. Kirsch, Lithium protects against cartilage degradation in osteoarthritis, Arthritis Rheum. 66 (5) (2014) 1228–1236.
[39] C.L. Thompson, H. Yasmin, A. Varone, A. Wiles, C.A. Poole, M.M. Knight, Lithium chloride prevents interleukin-1 induced cartilage degradation and loss of mechanical properties, J. Orthop. Res. 33 (10) (2015) 1552–1559.
[40] Y. Wu, S. Zhu, C. Wu, P. Lu, C. Hu, S. Xiong, J. Chang, B.C. Heng, Y. Xiao, H.W. Ouyang, A Bi-Lineage conducive scaffold for osteochondral defect regeneration, Adv. Funct. Mater. 24 (28) (2014) 4473–4483.
[41] C.L. Thompson, A. Wiles, C.A. Poole, M.M. Knight, Lithium chloride modulates chondrocyte primary cilia and inhibits Hedgehog signaling, FASEB J 30 (2) (2016) 716–726.
[42] M.E. Villafuertecastrejon, A. Dago, R. Pomes, Crystal-structure determination of $Li_2Ca_4Si_4O_{13}$, J. Solid State Chem. 112 (2) (1994) 438–440.
[43] T. Kokubo, H. Takadama, How useful is SBF in predicting in vivo bone bioactivity? Biomaterials 27 (15) (2006) 2907–2915.
[44] H. Zhu, D. Zhai, C. Lin, Y. Zhang, Z. Huan, J. Chang, C. Wu, 3D plotting of highly uniform Sr-5(PO4)(2)SiO4 bioceramic scaffolds for bone tissue engineering, J. Mater. Chem. B 4 (37) (2016) 6200–6212.
[45] C. Deng, Q. Yao, C. Feng, J. Li, L. Wang, G. Cheng, M. Shi, L. Chen, J. Chang, C. Wu, 3D printing of bilineage constructive biomaterials for bone and cartilage regeneration, Adv. Funct. Mater. (2017), 1703117.
[46] A.R. West, Phase equilibria in system Li2O-CaO-SiO2, J. Am. Ceram. Soc. 61 (3–4) (1978) 152–155.
[47] V. Karageorgiou, D. Kaplan, Porosity of 3D biomaterial scaffolds and osteogenesis, Biomaterials 26 (27) (2005) 5474–5491.
[48] M. Xu, D. Zhai, J. Chang, C. Wu, In vitro assessment of three-dimensionally plotted nagelschmidtite bioceramic scaffolds with varied macropore morphologies, Acta Biomater. 10 (1) (2014) 463–476.
[49] C. Wu, W. Fan, Y. Zhou, Y. Luo, M. Gelinsky, J. Chang, Y. Xiao, 3D-printing of highly uniform CaSiO3 ceramic scaffolds: preparation, characterization and in vivo osteogenesis, J. Mater. Chem. 22 (24) (2012) 12288–12295.
[50] C. Xin, X. Qi, M. Zhu, S.C. Zhao, Y.F. Zhu, Hydroxyapatite whisker-reinforced composite scaffolds through 3D printing for bone repair, J. Inorg. Mater. 32 (8) (2017) 837–844.
[51] Q. Fu, E. Saiz, M.N. Rahaman, A.P. Tomsia, Toward strong and tough glass and ceramic scaffolds for bone repair, Adv. Funct. Mater. 23 (44) (2013) 5461–5476.
[52] E. Tsuruga, H. Takita, H. Itoh, Y. Wakisaka, Y. Kuboki, Pore size of porous hydroxyapatite as the cell-substratum controls BMP-induced osteogenesis,

J. Biochem. (Tokyo) 121 (2) (1997) 317–324.
[53] W. Xiao, Y.M. Liu, K.G. Ren, F. Shi, Y. Li, W. Zhi, J. Weng, S.X. Qu, Evaluation of vascularization of porous calcium phosphate by chick chorioallantoic membrane model ex vivo, J. Inorg. Mater. 32 (6) (2017) 649–654.
[54] D. Tang, R.S. Tare, L.-Y. Yang, D.F. Williams, K.-L. Ou, R.O.C. Oreffo, Biofabrication of bone tissue: approaches, challenges and translation for bone regeneration, Biomaterials 83 (2016) 363–382.
[55] Y. Kawato, M. Hirao, K. Ebina, K. Shi, J. Hashimoto, Y. Honjo, H. Yoshikawa, A. Myoui, Nkx3.2 promotes primary chondrogenic differentiation by upregulating Col2a1 transcription, PLoS One 7 (4) (2012) e34703.
[56] C. Ferguson, E. Alpern, T. Miclau, J.A. Helms, Does adult fracture repair recapitulate embryonic skeletal formation? Mech. Dev. 87 (1) (1999) 57–66.
[57] D. Pfander, T. Cramer, E. Schipani, R.S. Johnson, HIF-1α controls extracellular matrix synthesis by epiphyseal chondrocytes, J. Cell Sci. 116 (9) (2003) 1819–1826.
[58] D.E. Komatsu, M. Hadjiargyrou, Activation of the transcription factor HIF-1 and its target genes, VEGF, HO-1, iNOS, during fracture repair, Bone 34 (4) (2004) 680–688.
[59] X.Y. Liu, C.X. Ding, P.K. Chu, Mechanism of apatite formation on wollastonite coatings in simulated body fluids, Biomaterials 25 (10) (2004) 1755–1761.
[60] L.L. Hench, Bioceramics - from concept to clinic, J. Am. Ceram. Soc. 74 (7) (1991) 1487–1510.
[61] C.T. Wu, Y. Ramaswamy, D. Kwik, H. Zreiqat, The effect of strontium incorporation into CaSiO3 ceramics on their physical and biological properties, Biomaterials 28 (21) (2007) 3171–3181.
[62] S. Xu, K. Lin, Z. Wang, J. Chang, L. Wang, J. Lu, C. Ning, Reconstruction of calvarial defect of rabbits using porous calcium silicate bioactive ceramics, Biomaterials 29 (17) (2008) 2588–2596.
[63] Y.-F. Chou, W. Huang, J.C.Y. Dunn, T.A. Miller, B.M. Wu, The effect of biomimetic apatite structure on osteoblast viability, proliferation, and gene expression, Biomaterials 26 (3) (2005) 285–295.
[64] N. Olmo, A.I. Martın, A.J. Salinas, J. Turnay, M. Vallet-Regi, M.A. Lizarbe, Bioactive sol–gel glasses with and without a hydroxycarbonate apatite layer as substrates for osteoblast cell adhesion and proliferation, Biomaterials 24 (20) (2003) 3383–3393.
[65] P. Pei, X. Qi, X.Y. Du, M. Zhu, S.C. Zhao, Y.F. Zhu, Three-dimensional printing of tricalcium silicate/mesoporous bioactive glass cement scaffolds for bone regeneration, J. Mater. Chem. B 4 (46) (2016) 7452–7463.
[66] H. Harada, S. Tagashira, M. Fujiwara, S. Ogawa, T. Katsumata, A. Yamaguchi, T. Komori, M. Nakatsuka, Cbfa1 isoforms exert functional differences in osteoblast differentiation, J. Biol. Chem. 274 (11) (1999) 6972–6978.
[67] K.S. Lee, S.H. Hong, S.C. Bae, Both the Smad and p38 MAPK pathways play a crucial role in Runx2 expression following induction by transforming growth factor-beta and bone morphogenetic protein, Oncogene 21 (47) (2002) 7156–7163.

Please cite this article in press as: L. Chen, et al., 3D printing of a lithium-calcium-silicate crystal bioscaffold with dual bioactivities for osteochondral interface reconstruction, Biomaterials (2018), https://doi.org/10.1016/j.biomaterials.2018.04.005